Energy & Environmental Science

ROYAL SOCIETY OF CHEMISTRY

PAPER

View Article Online
View Journal | View Issue

Cite this: *Energy Environ. Sci.*, 2020, **13**, 4269

Failure modes of protection layers produced by atomic layer deposition of amorphous TiO_2 on GaAs anodes†

Pakpoom Buabthong,[a] Zachary P. Ifkovits,[b] Paul A. Kempler,[b] Yikai Chen,[a] Paul D. Nunez,[b] Bruce S. Brunschwig,[c] Kimberly M. Papadantonakis[b] and Nathan S. Lewis *[bc]

Received 26th June 2020,
Accepted 23rd September 2020

DOI: 10.1039/d0ee02032j

rsc.li/ees

Amorphous titanium dioxide (a-TiO_2) films formed by atomic layer deposition can serve as protective coatings for semiconducting photoanodes in water-splitting cells using strongly alkaline aqueous electrolytes. Herein, we experimentally examine the mechanisms of failure for p^+-GaAs anodes coated with a-TiO_2 films (GaAs/a-TiO_2). Galvanic displacement of exposed GaAs by Au allowed imaging of pinholes in the a-TiO_2 coatings, and enabled collection of quantitative and statistical data associated with pinhole defects. A combination of imaging, electrochemical measurements, and quantitative analyses of corrosion products indicated that extrinsic pinholes were present in the a-TiO_2 films before electrochemical operation. During electrochemical operation these pinholes led to pitting corrosion of the underlying GaAs substrate. The dominant source of pinholes was the presence of atmospheric particulate matter on the GaAs surface during deposition of the a-TiO_2 layer. The pinhole density decreased substantially when the thickness of the a-TiO_2 coating increased beyond 45 nm, and approached zero when the thickness of the film exceeded 112 nm. The density of pinholes in films thinner than 45 nm decreased when the a-TiO_2 coating was deposited in an environmentally controlled cleanroom. Pinhole-free GaAs/a-TiO_2 devices were also tested *via* chronoamperometry to quantify the rate of pinhole formation during electrochemistry. The time-to-failure increased with thickness, suggesting that the failure mechanism may involve diffusion or migration through the film. However, other mechanisms may also contribute to the degradation of thicker films (>112 nm). Nevertheless, as previously hypothesized, extrinsic pinhole defects formed during deposition and testing control the short-term protective performance of the a-TiO_2 film for GaAs anodes evolving O_2 from water.

Broader context

Photoelectrochemical fuel generation allows energy from sunlight to be stored for later use. Many semiconducting materials corrode during operation such that long-term stability remains as one of the major challenges in the field. Protective coatings prepared from conductive metal oxides have been shown to substantially increase device lifetimes, but microscopic defects in the film can eventually lead to failure. We demonstrate herein the failure modes of amorphous titanium dioxide films prepared *via* atomic layer deposition and the deleterious effect on semiconductor substrates. This fundamental study will enable further systematic investigation of pinhole defects and the development of mitigation strategies needed to realize the practical implementation of stable photoelectrochemical solar fuel devices.

Introduction

Thick (~100 nm) films of amorphous-TiO_2 (a-TiO_2) formed by atomic layer deposition (ALD) have emerged as promising protective coatings for semiconducting photoanodes in photoelectrochemical (PEC) water-splitting and CO_2-reduction cells that contain strongly alkaline aqueous electrolytes.[1–4] a-TiO_2 coatings stabilize semiconducting photoanodes that form surface

[a] *Division of Engineering and Applied Sciences, California Institute of Technology, Pasadena, CA 91125, USA*
[b] *Division of Chemistry and Chemical Engineering, California Institute of Technology, Pasadena, California 91125, USA. E-mail: nslewis@caltech.edu*
[c] *Beckman Institute and Molecular Materials Research Center, California Institute of Technology, Pasadena, California 91125, USA*

† Electronic supplementary information (ESI) available. See DOI: 10.1039/d0ee02032j

oxides under water-oxidation conditions, such as Si and InP, as well as Group III–V materials that corrode by dissolving under water-oxidation conditions, such as GaAs and GaP.[1,5] The ability to stabilize materials that corrode by dissolution distinguishes a-TiO_2 from many other photoanode protection strategies and allows for the fabrication of III–V stacks of high efficiency monolithic tandem light absorbers. These tandem light absorbers are envisioned as the core of integrated solar fuels systems. Although a-TiO_2 films substantially increase the stability of water-splitting and CO_2-reduction cells with III–V photoanodes, their performance nevertheless degrades over time as manifested by a decrease in photocurrent density accompanied by corrosion of the substrate.[1,5,6] This degradation process has been hypothesized to result from pinhole defects that form during the deposition of the ALD films and/or during electrochemical operation of the electrodes protected by the ALD films.[5–7] Additionally, diffusion of OH^- through ALD a-TiO_2 films during PEC operation has been proposed as a mechanism for the formation of pinholes in a-TiO_2.[8,9]

Pinholes or other extrinsic defects formed during the deposition of a-TiO_2 on III–V or Group IV semiconductors have not yet been imaged, characterized or quantified. Pinholes have not been observed by scanning-electron microscopy (SEM) or atomic force microscopy (AFM) in freshly prepared thick coatings of a-TiO_2. Furthermore, plan-view images do not provide information on whether surface defects span the entire thickness of the film. If pinhole defects are the primary cause of failure of a-TiO_2 protective coatings, the ability to image and quantify pinhole defects is important for assessment of potential mitigation strategies to reduce the occurrence of pinholes in the films.

Pinhole defects formed in Al_2O_3 coatings during the ALD process have been studied for applications such as gas-diffusion barriers,[10] corrosion-resistant coatings,[11] and high-K gate dielectrics.[12] The origin of the pinholes is ascribed to the nature of the manufacturing process.[13] Pinholes in thicker films (>10 nm) typically arise from extrinsic contamination of the substrate, whereas pinholes in thinner films (<10 nm) typically are due to the ALD process itself, particularly, inefficient nucleation.[14] Analysis of microscopic pinhole defects in ALD layers is accomplished by first decorating the defects to amplify their visibility in subsequent imaging techniques. Examples of techniques used to amplify the visibility of defects include oxygen-plasma etching of the substrate,[15] electroplating metal,[16] or fluorescent tagging.[17] These techniques require that the film being studied is insulating, as is the case for Al_2O_3, and that the substrate is either conductive or a polymer, neither of which are applicable to III–V photoanodes coated with thick, a-TiO_2 protection layers.

Electroless gold deposition provides a simple process to deposit metallic contacts on functioning III–V semiconductor devices.[18] In the electroless process, the reduction of Au^{3+} in solution is paired to oxidation of the GaAs substrate. Consequently, galvanic displacement of GaAs by Au should provide high selectivity for the deposition of Au at sites where the GaAs substrate is exposed by film-spanning pinholes in thick, a-TiO_2 coatings, and should moreover provide a means to amplify the visibility of the defects by SEM.

Herein, we provide a detailed investigation of the stability of p^+-GaAs anodes protected by thick, a-TiO_2 coatings formed by (GaAs/a-TiO_2) in contact with 1.0 M KOH(aq). We demonstrate that galvanic displacement by Au is a useful technique to decorate pinholes, and use the technique to quantify the pinholes in the films and their dependence on the thickness of the a-TiO_2 film and the sample-preparation environment. We also examine the stability of a-TiO_2 films that were initially pinhole-free as indicated by the galvanic displacement and staining method.

Results and discussion

Corrosion of p^+-GaAs/a-TiO_2

For analysis of the onset potential for oxygen evolution, 2 nm of Ni was sputtered onto the surface of GaAs/a-TiO_2 electrodes prior to electrochemical testing. Fig. 1a shows the current

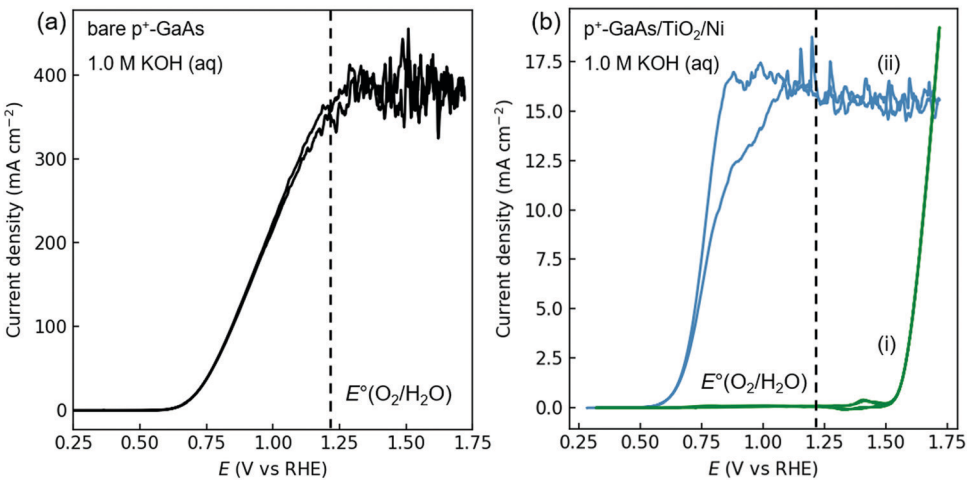

Fig. 1 Current density *vs.* potential (J–E) behavior of (a) bare p^+-GaAs and (b) two different p^+-GaAs samples coated with a-TiO_2-2000× (2000 ALD cycles) and sputtered Ni (GaAs/a-TiO_2-2000×/Ni). The scan rate was 40 mV s^{-1}. Two types of electrochemical behavior were observed for the GaAs/a-TiO_2-2000×/Ni samples prepared similarly: (i) no apparent corrosion current and (ii) substantial corrosion currents.

density *vs.* potential behavior of a bare p^+-GaAs electrode in contact with 1.0 M KOH(aq) in the dark. As the potential (E) was swept positive of 0.6 V *vs.* the reversible hydrogen electrode (RHE), the current density (J) increased from $\sim$0 mA cm^{-2} to $>$100 mA cm^{-2}. The observation of substantial current densities at $E < E^{\circ}(O_2/H_2O)$ is consistent with corrosive dissolution of the GaAs electrode. Fig. 1b compares representative J–E behavior for p^+-GaAs electrodes coated with a-TiO_2-2000$\times$ (2000 ALD cycles) and 2 nm of Ni (GaAs/a-TiO_2-2000$\times$/Ni) in contact with 1.0 M KOH(aq). Two types of electrochemical behavior were observed for the p^+-GaAs/a-TiO_2-2000$\times$/Ni electrodes: (i) negligible change in J until the Ni redox peaks appeared at $E \sim 1.4$ V *versus* RHE, followed by a steep rise in J near $E \sim 1.5$ V due to the onset of water oxidation, and (ii) a steep rise in J to $>$ 10 mA cm^{-2} near E = 0.6 V *versus* RHE, with J relatively constant for the rest of the anodic sweep. Similar electrochemical behaviors were also observed on the electrodes prepared without Ni (Fig. S1, ESI†), with the only differences being the absence of Ni redox peaks and water oxidation, suggesting that Ni does not substantially influence the corrosion kinetics of GaAs.

For the analysis of a-TiO_2 degradation, a-TiO_2-coated p^+-GaAs (with no Ni) substrates were used to minimize possible effects from the Ni overlayer that could confound interpretation of the corrosion kinetics of a-TiO_2, such as loss of catalyst or the Ni film forming an additional protective coating to the a-TiO_2. In an alkaline solution, GaAs substrates at open circuit undergo dissolution:

$$GaAs_{(s)} + 10OH^-_{(aq)} \rightarrow GaO_3{}^{3-}_{(aq)} + AsO_2{}^-_{(aq)} + 6e^- + 5H_2O_{(l)} \quad (1)$$

$$6H_2O_{(l)} + 6e^- \rightarrow 3H_{2(g)} + 6OH^-_{(aq)} \quad (2)$$

Fig. 2a–c shows J as a function of time for a bare p^+-GaAs electrode as well as for two different p^+-GaAs/a-TiO_2-1000$\times$ electrodes held at E = 1.13 V *vs.* RHE in contact with 1.0 M KOH(aq). Fig. 2d–f shows the concentration of dissolved Ga and As species in the electrolyte, as measured using ICP-MS, during the chronoamperometry experiments shown in Fig. 2a–c and the expected corrosion calculated based on the charge passed and six-electron oxidation of As as described in eqn (1). Fig. 2g–i shows scanning-electron micrographs (SEMs) of the

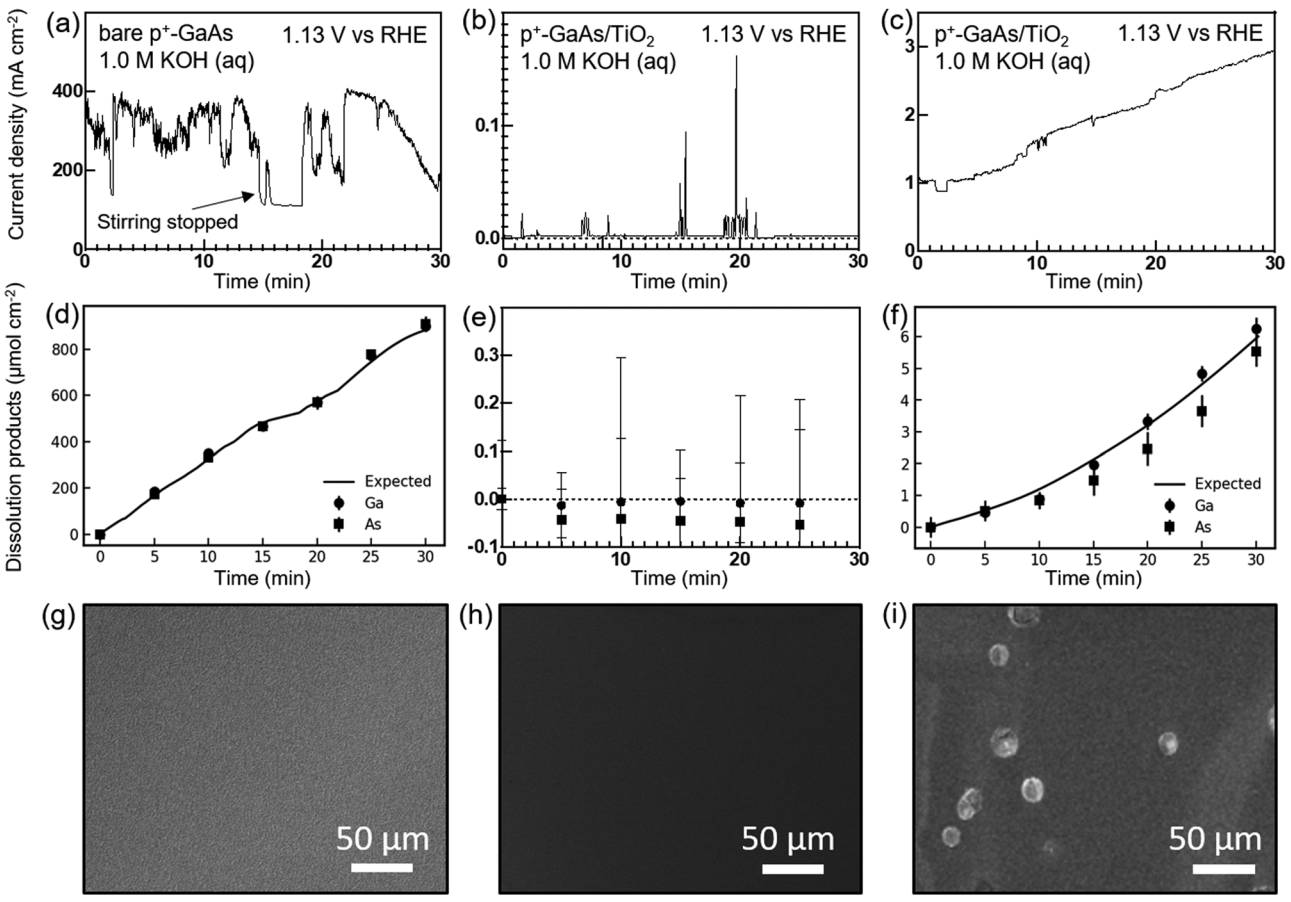

Fig. 2 Current density as a function of time in contact with 1.0 M KOH(aq) while held potentiostatically at E = 1.13 V *versus* RHE for (a) bare GaAs, and (b), (c) GaAs/TiO_2-1000$\times$ electrodes. In (b) and (c) samples, two different electrochemical behaviors were observed: (b) no apparent corrosion current and (c) corrosion current increases over time. (d)–(f) Concentrations of Ga and As species dissolved in the electrolytes over time as measured using ICP-MS during the experiments shown in (a)–(c) with the solid lines represent the expected dissolved GaAs calculated from the charge passed by the 6-electron GaAs dissolution. (g)–(i) SEMs of the electrodes after the 30 min chronoamperometry experiments shown in (a)–(c).

electrode surfaces after the chronoamperometry experiments shown in Fig. 2a–c.

For the bare GaAs electrode, J was initially 350 mA cm^{-2} and varied substantially with time, but remained $>$100 mA cm^{-2} throughout the 30 min experiment (Fig. 2a). The concentrations of both Ga and As species in the electrolyte increased linearly and stoichiometrically with time; the concentration of Ga and As species reached 900.2 $\pm$ 9.1 and 908.3 $\pm$ 8.1 μmol cm^{-2}, respectively, after 30 min of operation, in accord with the expected dissolution (Fig. 2d). After testing, the surface appeared roughened, but not pitted (Fig. 2g). Thus, the bare GaAs electrode corroded uniformly during the 30 min at E = 1.13 V *versus* RHE while in contact with 1.0 M KOH(aq). The variability in the current density observed over time likely resulted from changes in the active surface area of the GaAs during corrosion.

For a p$^+$-GaAs/a-TiO$_2$-1000$\times$ electrode that exhibited electrochemical behavior similar to type (i) in Fig. 1b, J was $\sim$0 mA cm^{-2} and remained constant through the 30 min of operation, although some transient peaks in current density that occurred during the brief obstruction of the electrode surface by bubbles in the electrolyte were observed (Fig. 2b). The concentrations of both Ga and As species in the electrolyte remained below the detection limit throughout the 30 min experiment (Fig. 2e), and the surface appeared unchanged after operation (Fig. 2h). Thus, no corrosion was evident after 30 min for this type of GaAs/a-TiO$_2$-1000$\times$ electrode.

A p$^+$-GaAs/a-TiO$_2$-1000$\times$ electrode that exhibited type (ii) electrochemical behavior is shown in Fig. 1b; J was initially $\sim$1 mA cm^{-2} but increased approximately linearly with time to $\sim$3 mA cm^{-2} after 30 min of operation (Fig. 2c). The concentrations of Ga and As species in the electrolyte increased with time but remained $\sim$100 times smaller than concentrations observed for the bare GaAs electrode, reaching 6.2 $\pm$ 0.4 μmol cm^{-2} for Ga and 5.5 $\pm$ 0.5 μmol cm^{-2} for As, in accord with the amount of dissolution calculated based on the charge passed and eqn (1) (Fig. 2f). After 30 min of operation, the electrode showed evidence of pitting (Fig. 2i).

The collective results of Fig. 1 and 2 demonstrate that when operated in contact with 1.0 M KOH(aq) at a potential less positive than $E^\circ(O_2/H_2O)$, some GaAs/a-TiO$_2$ samples undergo immediate pitting of the GaAs substrate (type ii), whereas other GaAs/a-TiO$_2$ samples exhibit no immediate evidence of corrosion (type i).

We hypothesized that the sites of pitting corrosion corresponded to pinhole defects that were randomly and sparsely distributed in the as-prepared ALD a-TiO$_2$ films. This would accordingly result in some pinhole-free GaAs/a-TiO$_2$ electrodes that exhibited stable electrochemical behavior and some GaAs/a-TiO$_2$ electrodes that contained pinholes and exhibited pitting corrosion. To confirm the existence of pinholes in the ALD a-TiO$_2$ films, galvanic displacement of GaAs by Au was used to tag the pinholes and amplify the contrast in the subsequent scanning-electron micrographs.

Electroless deposition of Au

Fig. 3a and b shows SEMs of a bare p$^+$-GaAs substrate before and after, respectively, galvanic displacement in an acidic solution containing 1 mM HAuCl$_4$(aq). After galvanic displacement, the surface of the sample was covered uniformly by Au (Fig. 3b). The Au film was then peeled off of the sample, and the appearance of the underlying GaAs substrate was consistent with uniform corrosion (Fig. 3c) due to the oxidative corrosion process of galvanic displacement. Fig. 3d shows an SEM of a p$^+$-GaAs/a-TiO$_2$-1000$\times$ sample that had been scribed and then subjected to galvanic displacement by Au. The Au selectively deposited at the exposed GaAs crevice. Moreover, no Au deposited galvanically onto an a-TiO$_2$ sample obtained by oxidizing a Ti foil (Fig. S2, ESI†), confirming the selectivity of the galvanic displacement for exposed GaAs sites on the GaAs/a-TiO$_2$ samples.

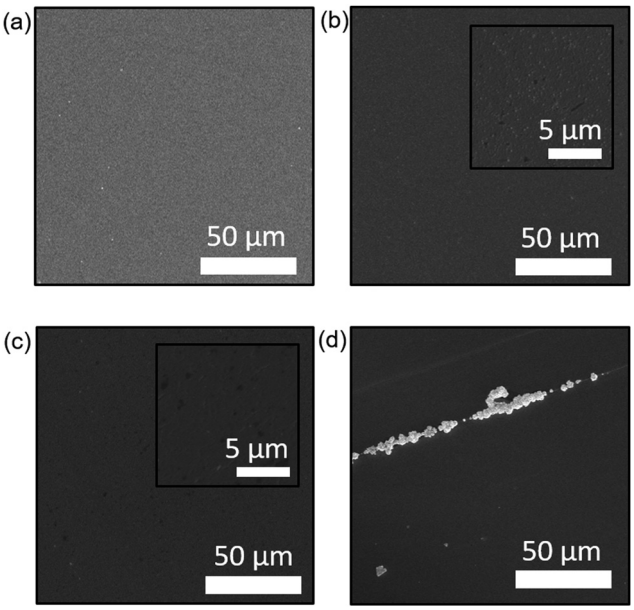

Fig. 3 Scanning-electron micrographs of (a) GaAs before deposition, (b) GaAs after Au deposition (c) GaAs after Au deposition with the Au film removed, and (d) a-TiO$_2$/GaAs with a line scratch after Au deposition.

Fig. 4a shows a cross-sectional SEM of a Au deposit formed on a p$^+$-GaAs/a-TiO$_2$-1000$\times$ sample after 30 min of galvanic displacement. The Au deposit had a fibrous, dendritic structure. Fig. 4b–d shows that as the duration of the galvanic displacement increased the amount of Au deposited increased. Fig. 5 also shows quantification of the density and diameters of the Au deposits. The number of Au spots per unit electrode surface area increased as the duration of the galvanic displacement reaction increased from 0 to $\sim$20 min (Fig. 5a). No new pinholes were decorated during the galvanic displacement process after $\sim$20 min and thereafter the spots increased in diameter until ultimately merging after 45 min (Fig. 5b). The exponential-like relationship between the diameter of Au deposits and the deposition time is consistent with a gradual increase in the average diameter in the beginning ($<$20 min) as more pinhole sites are being decorated. Once all pinholes have been decorated, a more rapid increase in the average diameter was observed, as expected when more surface area from the Au deposits is available for further deposition. The growth of the Au deposits with time is consistent with the fibrous nature of the Au deposits that allowed the Au solution to continue

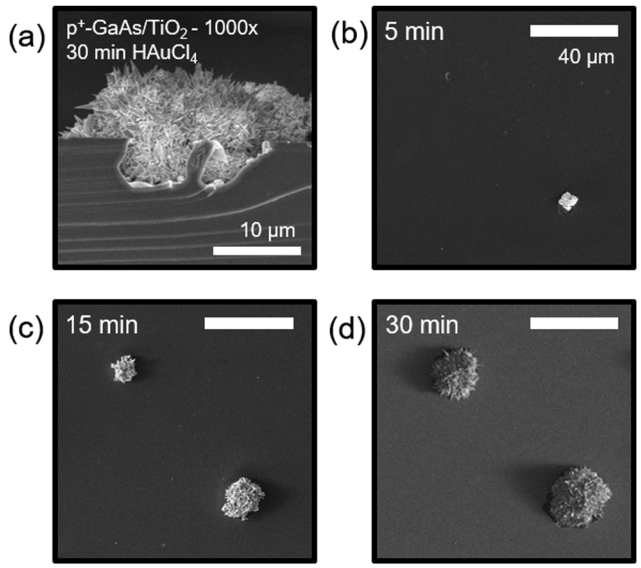

Fig. 4 Scanning-electron micrographs of (a) a cross section of a GaAs/a-TiO_2-1000× substrate after 30 min of galvanic displacement by Au. Plan-view images of Au deposits on the surfaces of GaAs/a-TiO_2-1000× samples after galvanic displacements for (b) 5, (c) 15, and (d) 30 min.

to contact and corrode the GaAs substrate. SEM images (Fig. 4b–d) showed that after 10 min of galvanic displacement the Au completely covered the portion of the GaAs exposed through the orifice in the a-TiO_2 film. This behavior implies that the diameters of the pinholes are proportional to the size of the Au spots.

Pinholes formed during a-TiO_2 deposition

To compare the size distribution of the pinholes, galvanic displacement of Au was applied to GaAs/a-TiO_2-1000× samples immediately after a-TiO_2 deposition. Fig. 5c shows the size distribution for 224 Au spots measured on GaAs/a-TiO_2-1000× samples after 10 min of galvanic displacement. The diameters of Au spots were sorted into 30 bins (~400 nm bin size), and the number of spots in each bin was counted. The ~400–800 nm bin contained the largest number of spots, exceeding by nearly 50% the number of spots in the next largest bin (~800–1200 nm). The distribution had a peak at ~800 nm, and a tail toward larger diameters. The average diameter of the Au spots was 1.8 ± 1.6 μm, for the 224 Au spots measured. The number and distribution of pinholes in a-TiO_2 layers of varied thickness was then analyzed using a Au deposition time of 30 min. Fig. 5d shows the density of Au spots on GaAs/a-TiO_2 after 30 min galvanic displacement as a function of a TiO_2 cycles.

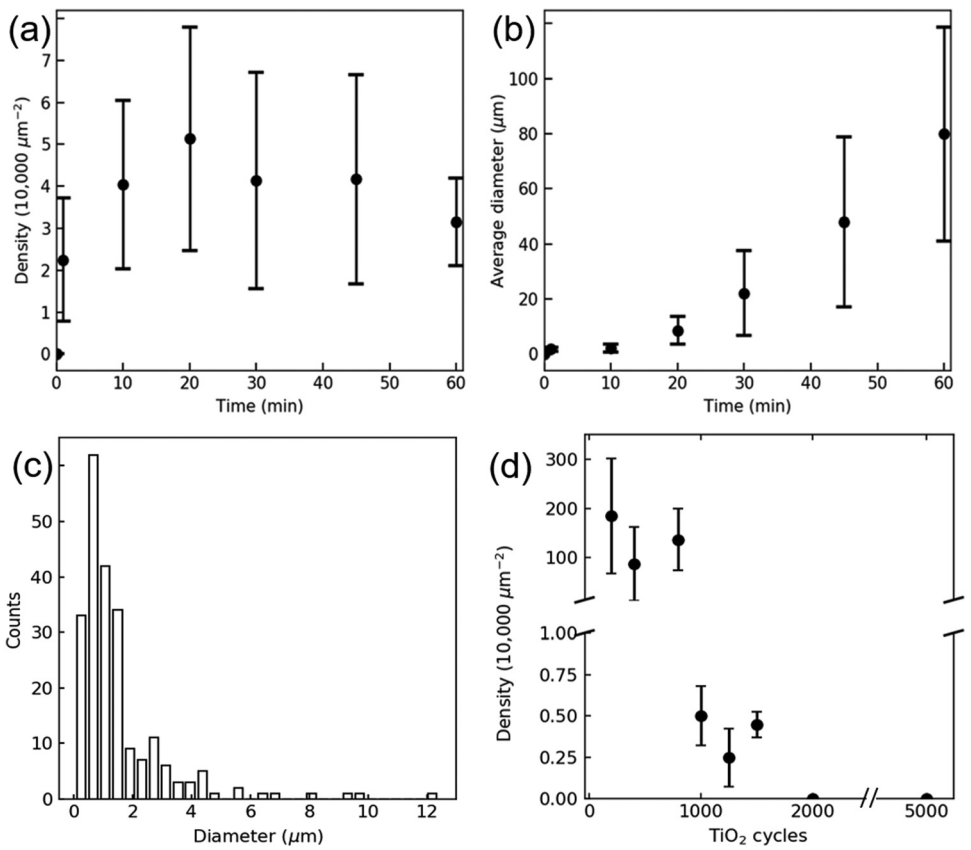

Fig. 5 (a) and (b) Analysis of Au spots observed on GaAs/1000×-a-TiO_2 as a function of the duration of galvanic displacement, showing (a) the average number of spots per unit electrode area, and (b) the average diameter of the Au spots on the surface in a 100 μm × 100 μm square. The error bars represent one standard deviation of the measurements from different areas of the electrode surface. (c) Distribution of the diameters of the plated Au spots after 10 min of deposition on 1000×-a-TiO_2/GaAs. (d) The density of Au spots on GaAs/a-TiO_2 samples after 30 min galvanic displacement as a function of the number of a-TiO_2 cycles.

The density of the pinholes decreased with the thickness of the a-TiO_2 film (Fig. 5d).

Pinholes were observed to form in ALD films both randomly and in clusters, leading to high variability in the pinhole density.[15] Although the mean value of the distribution of Au spots is considerably larger than the size distribution of the actual pinholes, the shape of the distribution, having a long tail toward larger diameters, is consistent with the hypothesis that the pinholes predominantly originate from external atmospheric particulates present during TiO_2 film deposition.[15,19] Moreover, the defect density decreased substantially after 800 cycles of a-TiO_2 ($\sim$45 nm), which could be a result of the a-TiO_2 film covering the majority of defects resulting from atmospheric particulate matter. The defect density continued to decrease with increases in thickness of the a-TiO_2 film, and approached zero after 2000 ALD cycles ($\sim$112 nm), indicating that a pinhole-free coating over the electrode area may be achieved at this thickness.

Fig. 6 compares the density of Au spots formed by galvanic displacement on GaAs samples covered with thin a-TiO_2 films (400 ALD cycles) to the Au spot density for a second set of samples grown using nominally the same deposition conditions but in a class-100 environmentally controlled cleanroom. The density of Au spots was much lower for the samples grown in the cleanroom (0.21 ± 0.14 counts per 10^4 μm^{-2}) than for samples grown outside the cleanroom (86.8 ± 74.9 counts per 10^4 μm^{-2}). This result clearly supports the hypothesis that the dominant source of pinholes in the a-ALD TiO_2 films is atmospheric particulates that are present during the deposition of the a-TiO_2.

Pinholes formed during electrochemical operation

For substrates that actively corrode under oxidizing conditions, such as III–V semiconductors, pinholes formed in protective coatings during the ALD process will have an immediate deleterious effect on the electrochemical stability of the protected semiconductor electrodes. However, additional pinholes might also form during electrochemical operation. Fig. 7a shows J measured as a function of time for a p^+-GaAs/a-TiO_2-2000$\times$ sample held at E = 1.13 V *versus* RHE while in contact with 1.0 M KOH(aq). After 8.2 h, J increased from $\sim$0 mA cm^{-2} to 0.19 mA cm^{-2}, and after another hour, J increased to 0.26 mA cm^{-2}. After $\sim$15 h of potential control, J increased steadily to $>$1.5 mA cm^{-2}. The initial lack of substantial corrosion current density implies that not all corrosion defects were initially present before the electrolysis, whereas the stepwise increase in the GaAs corrosion current density at 8.2 h suggests that either new defects can form over time or inactive defects can become activated during electrolysis. Exposure of the GaAs substrate after an electrochemical experiment is also consistent with the increase in the corrosion current observed in a J–E scan for a p^+-GaAs/a-TiO_2/Ni sample after 6 h of potential control (Fig. 7b). Similar behavior was also observed in a sample without Ni (Fig. S3, ESI†). Due to the irreversible nature of electroless Au deposition, imaging these pinholes formed during electrochemical testing would require an operando SEM and is beyond the scope of this work.

When a step increase in current density occurred, two different electrochemical behaviors were observed: (A) a large stepwise increase followed by a transient decay until the current density reached a new steady-state, and (B) a small stepwise increase followed by a continuous and gradual increase in current density. Fig. 7c shows a time window of Fig. 7a between 8.17 h and 8.87 h representing "A" behavior in which J increased from 0.05 mA cm^{-2} to 0.26 mA cm^{-2} followed by a decay to steady-state with J = 0.19 mA cm^{-2}. Fig. 7d shows a time window between 11.50 h and 12.20 h of Fig. 7a, representing "B" behavior, in which J increased from 0.298 mA cm^{-2} to 0.318 mA cm^{-2} followed by a small increase in J, and another stepwise increase from 0.321 mA cm^{-2} to 0.330 mA cm^{-2} followed by a continuous linear increase in J.

In "A" behavior, the transient decay indicates a decrease in corrosion rate after the initial spike, which likely indicates limited OH^- mass transport through pinholes (from the pinholes to the underlying etch pit). The mass transport of OH^- was evaluated using an axis-symmetric two-dimensional multiphysics model. The initial configuration of the sample contained a flat GaAs substrate, an insulating a-TiO_2 film with a fixed-diameter orifice, and bulk electrolyte on top of the

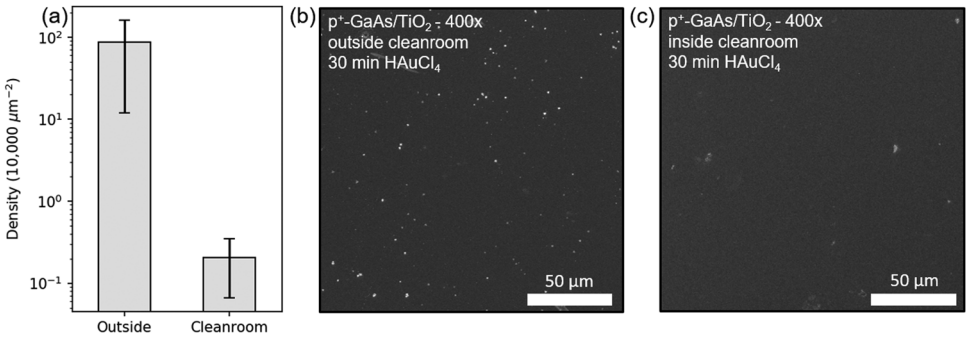

Fig. 6 (a) Comparison of the density of pinholes in a-TiO_2 films that were grown either inside or outside an environmentally controlled cleanroom. Samples were p^+-GaAs/a-TiO_2-400$\times$, and Au spots were counted after 30 min of galvanic displacement. Representative SEMs of samples prepared (b) outside the cleanroom, and (c) inside the cleanroom.

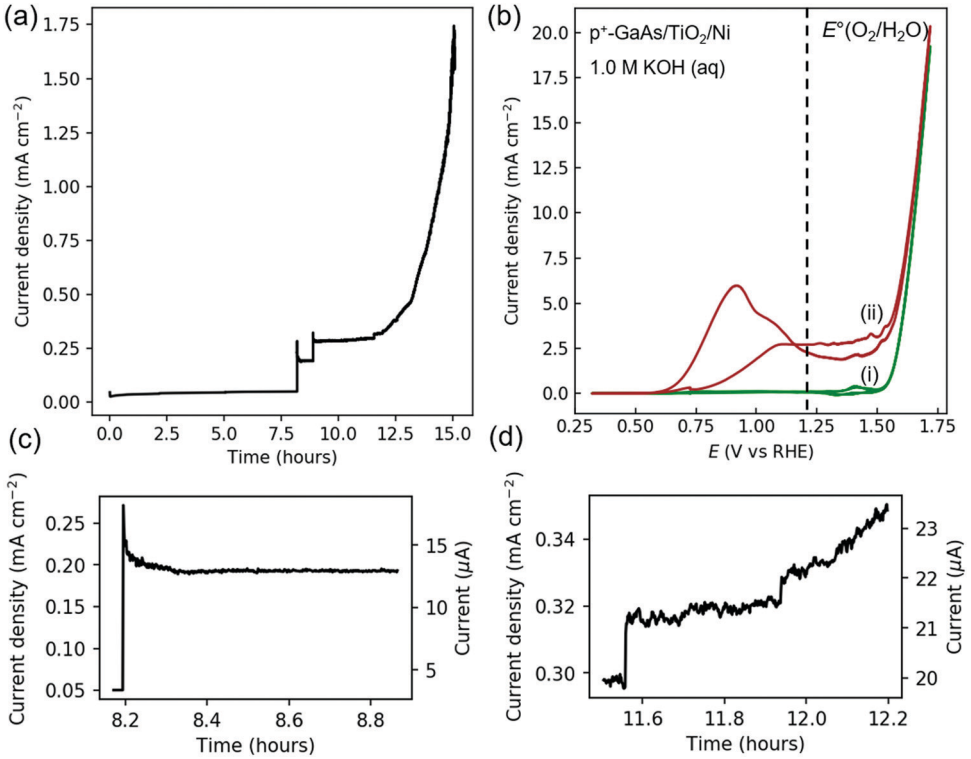

Fig. 7 (a) Current density as a function of time of GaAs/a-TiO_2-2000× held at 1.13 V *vs.* RHE in 1.0 M KOH(aq) (b) *J*–*E* behavior of p$^+$-GaAs samples coated with a-TiO_2 (2000 ALD cycles) and sputtered Ni (GaAs/a-TiO_2-2000×/Ni) at (i) 0 h and (ii) 6 h. The scan rate was 40 mV s^{-1}. (c) and (d) Current density as a function of time of GaAs/2000×-a-TiO_2 held at 1.13 V *vs.* RHE in 1.0 M KOH(aq) showing time window of Fig. 6a between (c) 8.17–8.87 hours and (d) 11.50–12.20 hours.

film (Fig. S4, ESI†). The transport of OH^- was governed by the Nernst–Plank equation and the continuity equation

$$\frac{\partial c_i}{\partial t} + \nabla \cdot J_i(x) = R_i$$
$$\frac{\partial c_i}{\partial t} + \nabla \cdot \left(-D_i \nabla c_i - z_i u_{m,i} F c_i \nabla V\right) = R_i \quad (3)$$

where $J_i(x)$, D_i, c_i, z_i, and $u_{m,i}$ are the flux, diffusion coefficient, concentration, charge number, and mobility, respectively, of species i within the electrolyte, and F, V, and R_i are the Faraday constant, the static electric field, and the chemical reaction rate of the corresponding species. In the simulation, the a-TiO_2 layer was modeled as an insulating layer. The anodic electrochemical reaction (eqn (1)) occurs at the interface between the electrolyte and GaAs. The kinetics of the reaction can be described with the concentration-associated anodic Tafel equation,

$$i = \frac{c_{OH^-}}{c^*_{OH^-}} i_0 \times 10^{\eta/A_a} \quad (4)$$

where c_{OH^-} and $c^*_{OH^-}$ represent the local and bulk OH^- concentration, respectively, A_a represents the anodic Tafel slope, η represents the overpotential, and i_0 represents the exchange-current density, which was set to 100 mA cm^{-2} to ensure facile corrosion kinetics and force mass-transport-controlled behavior in the simulation.

Fig. 8a shows the simulated current as a function of time for pinholes with four different radii but the same a-TiO_2 thickness (112 nm). For all pinhole sizes, the simulated current shows an initial transient spike that decays and reaches a steady state after a few seconds. Different pinhole radii lead to different maximum currents in the initial spike and steady-state electrolyte currents. The steady-state current increases with pinhole size, due to the decrease in OH^- diffusion resistance, whereas differences in the current of the initial spike are due to the amount of electrolyte that is contained in the pinhole. At the start of the simulation, the OH^- concentration at the GaAs surface is 1.0 M but rapidly decays and, with the depletion of the OH^- concentration within the pinhole, the current reaches a steady-state level controlled by the mass transport of OH^- through the pinhole. The time to reach a steady state in the simulation reflects the large assumed exchange-current density i_0 in eqn (4) that was used to maximize the corrosion kinetics and leads to rapid consumption of OH^- at the interface. The large i_0 is not meant to represent the observed rate. The magnitude of the initial and steady-state currents are close to those observed experimentally and the characteristic electrochemical behavior of the simulation is representative of the experimental observations. Fig. 8b and c shows the simulated concentration map of the concentration of OH^-, c_{OH^-}, in the electrolyte after 2.4 s of corrosion assuming a 3 μm radius pinhole. The value of c_{OH^-} at the surface of the corroding GaAs varies from 37 mM (near the intersection of the GaAs and

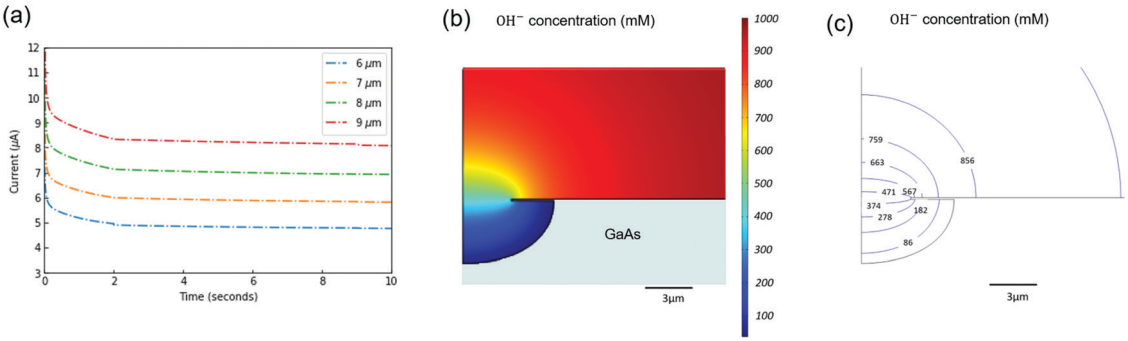

Fig. 8 (a) The simulated corrosion current as a function of time for different pinhole sizes with the thickness of a-TiO_2 fixed at 112 nm in the simulation. (b) Color map and (c) contour plot of the OH^- concentration in the electrolyte after 2.4 s of corrosion.

a-TiO_2 surface) to 50 mM (at the lowest point of the GaAs surface), and remains at 1.0 M in the bulk electrolyte away from the pinhole. A much smaller difference in the ratio of c_{OH^-} between the bulk electrolyte and the top of the pinhole also shows that, at 1.0 M, the transport of OH^- from the bulk electrolyte to the pinhole is not the main limiting factor. The steady-state current that appears within 2 s indicates that even with the facile GaAs corrosion kinetics (large i_0), the rate of corrosion is quickly dominated by the OH^- concentration gradient, and thus the mass transport, of OH^- through the orifice in the a-TiO_2 film. This behavior is consistent with the "A" behavior observed in Fig. 6a, where the opening of a new fixed-diameter pinhole leads to corrosion of the substrate.

In contrast, "B" behavior suggests a smaller initial pinhole, because of the smaller stepwise increase in J, but with a gradual increase in pinhole size as a function of time. The increase in the pinhole area likely comes from either expanding the diameter of the pinhole or its merging with nearby pinholes. After the formation of multiple pinholes, the merging of existing pinholes to form a larger channel can lead to an exponential increase in corrosion current as observed after 12.5 h of operation (Fig. 7a and d). These "A" and "B" corrosions can also be observed on a representative micrograph showing both ("A") spherical underlying etch pits with a fixed-diameter pinhole and ("B") merging pinholes (Fig. S5, ESI†). The current density continues to increase as more areas of GaAs are being etched until the electrolyte eventually reaches the back contact after 20 h, producing a very large stepwise increase in J (from $\sim$2.5 mA cm^{-2} to $\sim$15 mA cm^{-2} in Fig. 9a).

If all pinholes are separated, the first pinhole formed after 8.2 h would continue to etch isotopically with a fixed diameter, and $\sim$55 h would be required to etch through the substrate and reach back contact (see ESI† for calculation). However, the shorter time elapsed between the first pinhole formation and the electrolyte reaching the back contact ($\sim$20 h) is expected because merging of multiple pinholes leads to a larger exposed substrate area, representing a classic characteristic of corrosion by pitting.

Although extrinsic pinhole defects clearly constitute the predominant short-term failure mode of ALD a-TiO_2 protection layers, pinhole-free thick ALD a-TiO_2 films may still be subject to long-term failure processes. Fig. 9b shows an analysis of the time-to-failure as a function of the number of ALD cycles, where time-to-failure was defined as the time elapsed before the first increase in J for p^+-GaAs/a-TiO_2 samples held at E = 1.13 V *versus* RHE while in contact with 1.0 M KOH(aq). All a-TiO_2 films formed using <400 ALD cycles (>22 nm) on p^+-GaAs showed electrochemical evidence of initial pinholes. The time-to-failure increased substantially after 1500 cycles, showing that the time-to-failure depended on film thickness.

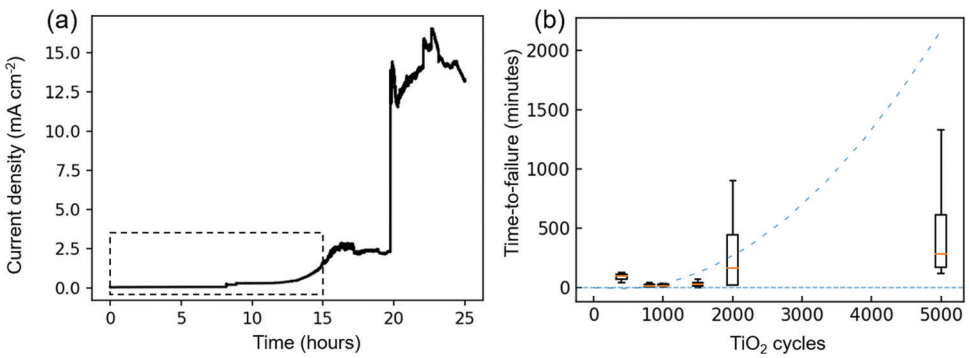

Fig. 9 (a) Current density as a function of time of GaAs/2000×-a-TiO_2 held at 1.13 V *vs.* RHE in 1.0 M KOH(aq) with the time extended to 25 h. The dashed box shows the region plotted in Fig. 7. (b) Elapsed time until the first step-wise increase in the current density as a function of a-TiO_2 cycles. The orange lines represent the medians; the box extends from the lower to the upper quartiles; the whiskers represent the range of the data. The blue long dashed line represents a fit of the data to a $[thickness]^2$ dependence using the data up to 2000 ALD TiO_2 cycles.

The dependence of time-to-failure on thickness is consistent with a mechanism involving transport of reactive species through the film, by either diffusion or migration, as has been proposed for a-TiO_2/Si.[8,9] To investigate the transport of reactive species, the oxygen profile in the a-TiO_2 was studied using XPS depth-profile analysis on pinhole-free p^+-GaAs/a-TiO_2-400× samples. The analysis was done on the region that did not show evidence of corrosion. Fig. S6 (ESI†) shows the area under the peaks for the Ti 2p, O 1s, Ga 3d, and As 3d signals, respectively, as a function of sputtering time on the samples before testing as well as after 1 h or 12 h of testing. In all three samples, Ga 3d and As 3d signals remained zero until ~600 min of sputtering time at which point the p^+-GaAs/a-TiO_2 interface was exposed. A slightly higher intensity for the Ga 3d and As 3d signals and lower intensity for the O 1s and Ti 2p signals in the first sputtering step are likely due to surface contamination and residues from the electrochemical experiment. Both the Ti 2p and O 1s signals slowly decreased from the beginning to ~200 min of sputtering time and continued to decrease again at ~600 min of sputtering time at the p^+-GaAs/a-TiO_2 interface.

No substantial compositional change was observed in the film after both 1 h and 12 h of testing. Ar-ion bombardment during the sputtering process has been shown to alter the Ti 2p spectrum leading to reduction of Ti^{4+} (to Ti^{2+}, Ti^{3+}), thus not accurately representing the underlying composition of TiO_2.[20] This behavior is representative of the initial decrease during the first ~200 min of sputtering time in all samples. To accurately quantify the transport of oxygen species through the film and to distinguish the oxygen arising from the electrolyte from oxygen in the a-TiO_2 film would require secondary ion mass spectrometry (SIMS) coupled with labeled oxygen isotopic analysis.

In addition, although the time-to-failure was observed to depend on the film thickness, the time-to-failure for p^+-GaAs/a-TiO_2-5000× (150–1200 min) films was shorter than expected (~2000 min) if diffusion through the a-TiO_2 were the only cause of the failure (Fig. 9b). Hence other mechanisms, such as local dissolution of the a-TiO_2 film or a degradation of the mechanical integrity of the a-TiO_2 film, likely contribute to the long-term failure of a-TiO_2 films as well. Further investigations of the mechanisms of degradation of a-TiO_2 films during long-term electrochemical operation are therefore required to fully understand and mitigate long-term failure of ALD a-TiO_2 protective coatings for oxygen-evolving photoanodes that undergo corrosion by dissolution. If the long-term failure mode is dominated by localized defective regions instead of an intrinsic property of an a-TiO_2 film, then isolating the defects and/or passivating the defective region to prevent further corrosion would increase the overall stability of the III–V devices. Evidence in support of intrinsic long-term durability of the a-TiO_2 is provided from the use of a-TiO_2 protection layers in the n-Si/a-TiO_2 system. The a-TiO_2 coating increased the stability of Si microwire photoanodes to >2200 h of continuous operation, attesting to the intrinsic long-term durability of protective a-TiO_2 films on photoanodes that are effecting the oxygen-evolution reaction.[3,21]

Conclusions

Pinhole defects in a-TiO_2 coatings formed during ALD lead to immediate failure and pitting corrosion of the underlying GaAs substrate when operated electrochemically in contact with 1.0 M KOH(aq). Galvanic displacement by Au facilitated imaging the sites of pinholes using scanning-electron microscopy, and enabled an analysis of the number of pinholes per unit electrode area, and of the dependence of the pinhole density on film thickness. The measurements and analyses suggest that the dominant source of pinholes in a-TiO_2 coatings is external atmospheric particulate matter present during the preparation and deposition steps. a-TiO_2 films with substantially lower pinhole densities were obtained when the thickness of the a-TiO_2 coating exceeded 45 nm, and nearly pinhole-free a-TiO_2 films could be fabricated when the a-TiO_2 thickness exceeded 112 nm. A similar result can also be achieved by careful preparation and a-TiO_2 film deposition in an environmentally controlled cleanroom. Long-term failure modes also exist in ALD a-TiO_2 films. Electrochemical measurements showed that pinholes can form or be exposed over time on electrodes that were initially pinhole-free. The time-to-failure increased as the thickness of the a-TiO_2 film increased, implying that transport of reactive species across the film could contribute to the failure of thick a-TiO_2 protective coatings that were initially nearly pinhole-free. Further understanding of the long-term failure mechanism, as well as differences between photoanodes that corrode *vs.* photoanodes that passivate, is required to rationally develop mitigation strategies that allow for extended long-term operation of protected photoanodes for evolution of O_2(g) from water.

Experimental

Materials and chemicals

Water with a resistivity $\rho > 18$ MΩ cm obtained from a Barnstead Millipore purification system was used throughout. All chemicals, including hydrochloric acid (ACS Grade, VWR), potassium hydroxide (TraceSELECT, ≥30% in water, Honeywell Fluka), and gold(III) chloride hydrate $HAuCl_4$ (~50%, Chem-Impex International Inc.) were used as received unless otherwise noted. Crystalline single-side polished GaAs substrates, p^+-GaAs(100) (350 ± 25 μm), were degenerately doped with zinc to a majority-carrier density of 0.5–5 × 10^{19} cm^{-3} (AXT Inc.).

Preparation of substrates

The GaAs wafers were cleaned with 10% HCl(aq) for 30 min to the remove native oxide on the surface.[22] The samples were then rinsed with copious amounts of deionized H_2O and dried using a stream of N_2(g).

Atomic-layer deposition (ALD) of TiO_2 thin films

a-TiO_2 films were grown using tetrakis(dimethylamido)-titanium (TDMAT). For TiO_2 films prepared from the TDMAT precursor, a Cambridge Nanotech S200 or Oxford Instruments FlexAL ALD system was used for deposition outside and inside the

cleanroom. Each ALD cycle consisted of a 0.10 s exposure to TDMAT (Sigma-Aldrich, 99.999%), a N_2(g) (Airgas, 99.999%) purge, a 0.015 s exposure to H_2O, and a final N_2(g) purge. Research grade 20 sccm N_2(g) was used for the N_2(g) purges, and each N_2(g) purge was 15 s in duration. During the deposition, the substrate and the TDMAT precursor were heated to 150 °C and 75 °C, respectively, while the H_2O remained at room temperature. Most samples were prepared with 400 cycles and 1000 ALD cycles, producing a nominal thickness of 22 nm and 55 nm, respectively. The film thickness and refractive index were measured *via* spectroscopic ellipsometry (J.A. Woollam Co., alpha-SE) and were fit to a Cauchy model.

Radio-frequency sputtering deposition

A radio-frequency sputtering system (AJA International Inc.) was used to deposit Ni and Cu for preparation of oxygen-evolution reduction (OER) catalysts as well as to produce back ohmic contacts to p^+-GaAs. The base pressure was kept at $<1 \times 10^{-7}$ Torr, and the deposition pressure was kept at 5 mTorr. A radio-frequency (rf) power of 100 W during the deposition.

Electrode fabrication

Electrodes were fabricated by using a scribe to cleave the samples into $\sim$0.1 cm^2 pieces. Ohmic contact was made by sequentially depositing Ni/Cu films onto the unpolished back sides of the p^+-GaAs samples.[1] The back contact to the sample was affixed to a Cu wire with Ag paste. The Cu wire was threaded through a glass tube (Corning Incorporation, Pyrex tubing, 7740 glass), and all but the front of the sample was encapsulated with Loctite epoxy (Hysol 9462). After curing, the electrode was scanned with an Epson scanner (V19) and analyzed with ImageJ software, to determine the area of the exposed region.

Scanning-electron microscopy

Scanning-electron micrographs (SEMs) were obtained with an FEI Nova NanoSEM 450 at an accelerating voltage of 5.00 kV with a working distance of 5 mm and an in-lens secondary electron detector.

Inductively coupled plasma mass spectroscopy

Inductively coupled plasma mass spectrometry (ICP-MS) data were collected using an Agilent 8800 Triple Quadrupole ICP-MS system. ICP-MS samples were collected periodically throughout electrochemical corrosion experiments. Samples were diluted 50× with 2% nitric acid before analysis. ICP-MS concentration standards were made with serial dilutions of a known concentration standard (Sigma-Aldrich) with 2% nitric acid. Each concentration standard had KOH added in a 50 : 1 volumetric ratio of nitric acid : KOH (2%, 1.0 M, respectively) to match the solution matrix of the ICP-MS samples. Quantification was verified by independently making four additional samples of known concentration, two for As and two for Ga, and analyzing them at the beginning, middle, and end of all ICP-MS analysis. ICP-MS results were only used when the samples of known concentration were measured to be consistent throughout the ICP-MS run. The samples of known concentration were also made on a mass basis and were matrix-matched with the same 50 nitric acid : 1 KOH volumetric ratio as both the unknown samples and the concentration standards. The total amount of dissolved Ga and As from the electrodes was then calculated and normalized to the geometric electrode area.

X-ray photoelectron spectroscopy

X-ray photoelectron spectroscopy (XPS) was performed using a Kratos Axis Ultra system with a base pressure of 1×10^{-9} Torr in the analysis chamber. A monochromatic Al Kα source was used to irradiate the sample with X-rays (1486.7 eV) at 150 W. For depth profiling, Ar^+ ions with an energy of 2 keV were used. A hemispherical analyzer oriented for detection along the sample surface normal was used for maximum depth sensitivity. Depth profile spectra were acquired with a pass energy of 160 eV and acquisition time of 20 seconds each. The data were analyzed using CasaXPS computer software.

XPS data were obtained *ex situ i.e.*, after a short sample transfer through air, which could potentially confound linking the surface composition and oxidation states found in UHV to the ones present during electrochemistry.

Electroless gold deposition

Electrodes were immersed in 10 mL of 1.0 M HCl(aq) for 1 min, then 10 mL of a 2 mM $HAuCl_4$ stock solution was added to the solution to produce a nominal concentration of 1 mM $HAuCl_4$.[18] Unless noted otherwise, all depositions were performed for 30 min at open circuit.

Image processing and pinhole density calculation

Scanning-electron micrographs of the surface after galvanic displacement of Au were analyzed using ImageJ software, with each processing step shown in Fig. S7 (ESI†). First, the raw image was converted into an 8-bit image. The image was then further converted into a black/white image with a specific threshold. The threshold was adjusted in each image depending on its contrast and brightness to include all gold deposits. The built-in particle analysis function was used to obtain the counts and the size distribution of the particles.

Electrochemical characterization

Electrochemical data were obtained using a BioLogic SP-200 potentiostat in a three-electrode configuration with 1.0 M KOH(aq) as the electrolyte, and a Hg/HgO electrode (CH Instruments, Inc., CHI-152) was used as the reference electrode for the alkaline solution. A carbon rod (Strem Chemicals, 99.999%) inside a porous fritted gas dispersion tube (Sigma Aldrich, Z408727) was used as the counter electrode. *J–E* data were collected between −0.6 V and 0.8 V *vs.* Hg/HgO at a 20 mV s^{-1} scan rate. Chronoamperometry (CA) data were collected every 1 s while holding the electrode potential at 0.212 V *vs.* Hg/HgO, unless noted otherwise. For a study of pinhole-free TiO_2 films, the chronoamperometry at 0.212 V *vs.* Hg/HgO from the first 1 min was closely monitored and had to exhibit a stable current density below 1 mA cm^{-2}.

Simulation of an etched pit

The electrolyte was modeled as a stagnant liquid, in which transport of electrolyte species was controlled by the diffusion and migration terms in the Nernst–Planck equation and the continuity equation (eqn (3)) and the corrosion kinetics by the Tafel equation (eqn (4)). The anodic Tafel slope, A_a, and the overpotential, η, were taken to be 120 mV dec^{-1} and 300 mV respectively. At each time step, the consumption of OH^- at the surface was calculated by Faraday's law using the current density from the previous time step (eqn (4)). The addition of OH^- was then calculated using eqn (3). Then, the current density at the surface was re-calculated from the new OH^- concentration, c_{OH^-}.

As time passes, the chemical etching on GaAs takes place with a velocity in the normal direction, v, according to

$$v = \frac{i}{6F}\frac{M}{\rho} \quad (5)$$

where M is the molar mass (145 g mol^{-1}) and ρ is the density (5320 kg m^{-3}) of gallium arsenide.

The OH^- concentration is fixed at 1 M on the top surface of the electrolyte domain, which accounts for the solution mixing. The cathode was set far apart from the anode and is not shown in Fig. S4 (ESI†).

The standard FEM solver in the COMSOL multi-physics package was used to obtain the modeled electrochemical behavior. The maximum element size and the maximum element growth rate for this 2-D axis-symmetric model were 72 nm and 1.1, respectively, for the region near the electrolyte electrode interface, and were 1.4 μm and 1.2, respectively, for the rest of the system. A relative tolerance of the corresponding variable of 0.001 was applied as the convergence criterion for all simulations.

Conflicts of interest

There are no conflicts of interest to declare.

Acknowledgements

This material is based upon work performed by the Joint Center for Artificial Photosynthesis, a DOE Energy Innovation Hub, supported through the Office of Science of the U.S. Department of Energy under Award Number DE-SC0004993. We gratefully acknowledge a gift from the Lam Research Unlock Ideas program. Deposition of a-TiO_2 in a cleanroom was performed in the Kavli Nanoscience Institute (KNI) at Caltech, and we thank the KNI staff for their assistance during fabrication.

References

1 S. Hu, M. R. Shaner, J. A. Beardslee, M. Lichterman, B. S. Brunschwig and N. S. Lewis, *Science*, 2014, **344**, 1005–1009.
2 X. Zhou, R. Liu, K. Sun, Y. Chen, E. Verlage, S. A. Francis, N. S. Lewis and C. Xiang, *ACS Energy Lett.*, 2016, **1**, 764–770.
3 M. R. Shaner, S. Hu, K. Sun and N. S. Lewis, *Energy Environ. Sci.*, 2015, **8**, 203–207.
4 M. F. Lichterman, A. I. Carim, M. T. McDowell, S. Hu, H. B. Gray, B. S. Brunschwig and N. S. Lewis, *Energy Environ. Sci.*, 2014, **7**, 3334–3337.
5 E. Verlage, S. Hu, R. Liu, R. J. R. Jones, K. Sun, C. Xiang, N. S. Lewis and H. A. Atwater, *Energy Environ. Sci.*, 2015, **8**, 3166–3172.
6 D. Bae, B. Seger, P. C. K. Vesborg, O. Hansen and I. Chorkendorff, *Chem. Soc. Rev.*, 2017, **46**, 1933–1954.
7 D. Bae, S. Shayestehaminzadeh, E. B. Thorsteinsson, T. Pedersen, O. Hansen, B. Seger, P. C. K. Vesborg, S. Ólafsson and I. Chorkendorff, *Sol. Energy Mater. Sol. Cells*, 2016, **144**, 758–765.
8 Y. Yu, C. Sun, X. Yin, J. Li, S. Cao, C. Zhang, P. M. Voyles and X. Wang, *Nano Lett.*, 2018, **18**, 5335–5342.
9 C. Ros, N. M. Carretero, J. David, J. Arbiol, T. Andreu and J. R. Morante, *ACS Appl. Mater. Interfaces*, 2019, **11**, 29725–29735.
10 A. A. Dameron, S. D. Davidson, B. B. Burton, P. F. Carcia, R. Scott McLean and S. M. George, *J. Phys. Chem. C*, 2008, **112**, 4573–4580.
11 A. I. Abdulagatov, Y. Yan, J. R. Cooper, Y. Zhang, Z. M. Gibbs, A. S. Cavanagh, R. G. Yang, Y. C. Lee and S. M. George, *ACS Appl. Mater. Interfaces*, 2011, **3**, 4593–4601.
12 H. Spahr, T. Bülow, C. Nowak, F. Hirschberg, J. Reinker, S. Hamwi, H. H. Johannes and W. Kowalsky, *Thin Solid Films*, 2013, **534**, 172–176.
13 K. Lahtinen, J. Lahti, P. Johansson, T. Seppänen and D. C. Cameron, *J. Coat. Technol. Res.*, 2014, **11**, 775–784.
14 Y. Zhang, D. Seghete, A. Abdulagatov, Z. Gibbs, A. Cavanagh, R. Yang, S. George and Y.-C. Lee, *Surf. Coat. Technol.*, 2011, **205**, 3334–3339.
15 A. S. Yersak and Y.-C. Lee, *J. Vac. Sci. Technol., A*, 2016, **34**, 01A149.
16 Y. Zhang, J. A. Bertrand, R. Yang, S. M. George and Y. C. Lee, *Thin Solid Films*, 2009, **517**, 3269–3272.
17 Y. Zhang, Y. Z. Zhang, D. C. Miller, J. A. Bertrand, S. H. Jen, R. Yang, M. L. Dunn, S. M. George and Y. C. Lee, *Thin Solid Films*, 2009, **517**, 6794–6797.
18 M. R. Hormozi Nezhad, M. Aizawa, L. A. Porter, A. E. Ribbe and J. M. Buriak, *Small*, 2005, **1**, 1076–1081.
19 W. E. Clark and K. T. Whitby, *J. Atmos. Sci.*, 1967, **24**, 677–687.
20 S. Hashimoto and A. Tanaka, *Surf. Interface Anal.*, 2002, **34**, 262–265.
21 M. R. Shaner, K. T. Fountaine, S. Ardo, R. H. Coridan, H. A. Atwater and N. S. Lewis, *Energy Environ. Sci.*, 2014, **7**, 779–790.
22 F. Yang, A. C. Nielander, R. L. Grimm and N. S. Lewis, *J. Phys. Chem. C*, 2016, **120**, 6989–6995.